TEL AVIV UNIVERSITY

The Iby and Aladar Fleischman Faculty of Engineering

The Zandman-Slaner School of Graduate Studies

Ultrasound-Compatible Microfluidic Platform for In Vitro Microvasculature Flow Research and Ultrasound Localization Microscopy

A thesis submitted toward the degree of

Master of Science in Biomedical Engineering

by

Tamar Mano

This research was carried out in the Department of Biomedical Engineering

Under the supervision of Dr. Tali Ilovitsh

TEL AVIV UNIVERSITY

The Iby and Aladar Fleischman Faculty of Engineering

The Zandman-Slaner School of Graduate Studies

Ultrasound-Compatible Microfluidic Platform for In Vitro Microvasculature Flow Research and Ultrasound Localization Microscopy

A thesis submitted toward the degree of

Master of Science in Biomedical Engineering

by

Tamar Mano

This research was carried out in the Department of Biomedical Engineering

Under the supervision of Dr. Tali Ilovitsh

Acknowledgments

I would like to thank my supervisor Dr. Tali Ilovitsh, for her unwavering support and mentorship throughout this project. Thank you for your constant guidance and confidence in this research.

I would like to thank my friends and family for always encouraging me and pushing me to succeed.

Abstract

Ultrasound localization microscopy (ULM) is used to create super-resolved images and velocity maps by localizing and tracking microbubble contrast agents through a vascular network over thousands of frames of ultrafast plane wave images. However, a significant challenge lies in developing ultrasound-compatible microvasculature phantoms to investigate microbubble flow and distribution in controlled environments. To overcome this challenge, we introduce a new class of gelatin-based microfluidic-inspired phantoms, uniquely tailored for ULM studies. These novel phantoms allow for the creation of complex and reproducible microvascular networks, featuring channel diameters as small as 100 μm. Our microfluidic-inspired phantoms can be used to create a variety of networks that can be repetitively imaged and analyzed. Here, we study the behavior of microbubbles (MBs) under ULM conditions within bifurcating and converging vessel phantoms. First, the effect of bifurcation angle (25°,45°, and 55°) and flow rate (0.01, 0.02, and 0.03 ml/min) on time to full acquisition of branching channels were evaluated. Additionally, we explore the saturation time effect of narrow channels branching off larger ones. Longer acquisition time was required for the narrow vessel, with an average increase of 72% for 100 μm channel branching off a 300 μm channel, and an average increase of 90% for a 200 μm channel branching off a 500 μm channel. The robustness of our fabrication method is demonstrated through the creation of two trifurcating microfluidic phantoms, including one that converges back into a single channel, a configuration that cannot be achieved through traditional methods. This new class of ULM phantoms serves as a versatile platform for noninvasively studying complex flow patterns using ultrasound imaging, unlocking new possibilities for in vitro microvasculature research and imaging optimization.

Table of Contents

Abbreviations and Symbols

US ..... Ultrasound

ULM ..... Ultrasound localization microscopy

CNC ..... Computer numerical control

CPS ..... Contrast pulse sequence

FWHM ..... Full width half max

MB ..... Microbubble

NB ..... Nanobubble

MI ..... Mechanical index

PNP ..... Peak negative pressure

PSF ..... Point spread function

PW ..... Plane wave

RF ..... Radio frequency

ROI ..... Range of interest

SVD ..... Singular value decomposition

TIS ..... Thermal index

τ ..... Saturation time

List of Tables

List of Figures

List of Publications

- **T. Mano**, T. Grutman, and T. Ilovitsh. Versatile Ultrasound-Compatible Microfluidic Platform for In Vitro Microvasculature Flow Research and Imaging Optimization. ACS Omega (2023). Conducted all of the research: Developed and fabricated the microfluidic platform, performed all of the experiments, implemented the post processing code, and conducted data analysis and paper writing.
- M. Bismuth, S. Katz, **T. Mano**, R. Aronovich, D. Hershkovitz, A. Exner and T. Ilovitsh. Low frequency nanobubble-enhanced ultrasound mechanotherapy for noninvasive cancer surgery. Nanoscale (2022). Wrote the ultrasound image acquisition protocol and assisted in experiments.

Conference presentations:

T. Mano, T. Grutman, and T. Ilovitsh. “Flow characterization in branching vessels using a microfluidic-inspired phantom and ultrasound localization microscopy”, ISTU, April 2023 (Oral presentation).

1 Introduction

Ultrasound (US) is a widely used medical diagnostics technique enabling real-time imaging, accounting for about one in four of all medical imaging procedures completed worldwide. US is commonly used for imaging soft tissues anatomy and physiology such as the liver, kidney, breast, heart, and muscular and vascular systems. US has many advantages compared to other commonly used imaging modalities, such as its low cost in comparison to MRI and lack of ionizing radiation when compared to X-Ray, PET, and CT [1]. When performed according to regulations, the chances of an US imaging procedure causing thermal or mechanical damage or any other adverse bioeffects are very low [2].

The basic concept of US imaging leans on applying an electrical voltage to a piezoelectric element which vibrates at a certain frequency in response to an alternating current. The pressure wave produced propagates through the tissue being imaged, where it is absorbed, reflected, and scattered back to the piezoelectric element. The returning pressure wave is received by the piezoelectric element and converted back to voltage, which is sampled and forms the raw data signal. An US transducer consists of an array of piezoelectric elements that transmit and receive sound waves, and can be used to reconstruct a full image of the tissue [3].

US imaging can be divided into standard linear imaging and nonlinear imaging. Historically, linearity is a fundamental assumption of the US imaging system. However, most tissues are nonlinear- this means that the shape and amplitude of the signal received by the US transducer is not perfectly proportional to the shape and amplitude of the transmitted pulse [4]. Contrast agents in the form of gas-filled microbubbles (MBs) and nanobubbles (NBs) encapsulated in phospholipid shells are known to have a strong non-linear response to US pressure waves. Harmonic imaging sequences can be used to enhance the non-linear effect by

detecting harmonic frequencies returned from the non-linear MB contrast agents and zeroing out the signal received from linear scatterers such as soft tissues and fluid [5].

MBs can be injected into the blood stream where they enhance the received signal and create high contrast images of blood vessels within the body. MBs act as point scatterers and are smaller than the diffraction limit of the US system, therefore they appear as the point spread function (PSF) of the system, which is on the range of 0.5 mm for conventional US imaging. As a result, smaller features cannot be resolved, which poses a substantial limit on the ability image individual blood vessels and form a detailed image of the microvascular system. In an equivalent approach to optical localization microscopy methods such as PALM, FPALM, and STORM [6], ultrasound localization microscopy was demonstrated by individually localizing and tracking MBs flowing through the blood stream to form super-resolved microvascular images and velocity maps [7].

Research in the field of ultrasound localization microscopy (ULM) imaging is rapidly growing, with studies exploring various fields such as localization and tracking algorithms [8] and different contrast agents [9]. New methods and materials may be tested and validated using computerized simulations, tissue-mimicking phantoms, and in vivo studies. Engineering complex tissue-mimicking vascular flow phantoms is a challenge, with most phantoms relying on single channels embedded in agar or gelatin [10][11]. The purpose of this study is to provide a simple, cost-effective solution to engineering micro-vascular flow phantoms and use the proposed phantoms to study flow in a variety of vascular structures using US contrast agents. We validate the ability to accurately reconstruct images and velocity maps of channels within the microvascular networks in the phantoms, and tested different microvasculature configurations. In addition, ULM acquisition time was reported to be significantly longer in small vessels due to

limited MB access and slower blood flow[12]. We first used in-vivo data from a rat kidney to confirm this observation. Then, we used the US compatible microvasculature phantoms to study the physical properties of bubble flow and distribution, while assessing the impact of channel width, bifurcation angle and flow rate on ULM acquisition. Lastly, to improve ULM in small blood vessels, we used nanoscale contrast agents, NBs. Our platform showed that the use of these echogenic NBs improves ULM acquisition time in small channels, compared to MBs.

2 Research Objectives

This work aims to develop and utilize a platform for controlled ULM imaging. By creating tissue-mimicking microfluidic devices that are compatible with high frequency ultrasound imaging, we are able to statistically analyze microbubble contrast agent behavior as they flow through complex channels under ultra-fast frame rate conditions. The first goal was to fabricate a phantom using ultrasound compatible materials that is cost-effective, easily reproducible, and capable of creating a wide range of microvascular structures with diameters that mimic those of blood vessels. In order to simulate flow conditions, the device needed to be easily attached to a programable flow pump and imaged using a standard linear ultrasound transducer.

The next goal was to perform US experiments using this device and develop a robust post-processing algorithm to study important aspects of MB flow. A major challenge in ULM imaging is the long acquisition time needed to form an entire image in-vivo. Here, we tested acquisition time in a controlled environment to gain a better understanding of the effect of a range of variables on saturation time in bifurcating vessels.

3 Theoretical Background

3.1 Ultrasound imaging principles

Ultrasound imaging utilizes sound waves with frequencies higher than 20 kHz, extending beyond the range of human hearing. It is an acoustic wave that propagates through the expansion and compression of a medium, traveling at the speed of sound, which varies depending on the specific medium. Initially employed for sonar and radar applications, ultrasound technology was later suggested for medical purposes after World War II. In contrast to sonar and radar, which primarily detect solid targets in bodies of water like ships, medical ultrasound focuses on generating images of soft tissues within the human body. Both approaches acquire spatial information about a region or object within a medium by receiving the backscattered acoustic signals emitted by the transmitted sound waves [3].

In standard medical ultrasound imaging, a transducer is utilized to convert electrical signals into acoustic signals at a specific center frequency. The transducer emits short acoustic pulses into the human body. The body comprises various tissues with different acoustic properties, making it inhomogeneous. At each point within the tissue, the acoustic pulses, also known as ultrasound waves, can be reflected, scattered, and/or transmitted. Consequently, "echo" waves are generated and propagate back toward the transducer. The transducer receives these echoes and converts them back into electric signals. The electric signal is then processed to generate an image of the tissue, where each point in the image corresponds to an anatomical location within the tissue and the brightness of the point corresponds to the strength of the backscattered echo [1].

As sound waves travel through tissues, there are a few factors that affect the final contrast achieved between different tissues in the resulting image. The most important factor is acoustic

impedance. Impedance is defined as the resistance to the propagation of a sound wave. For example, at the interface between two surfaces consisting of different tissues, reflection of the wave occurs due to impedance. The intensity of the wave that is reflected is proportional to the change in acoustic impedance between the two tissues. Certain materials such as gas and bone have very high acoustic impedance, reflecting a large portion of the propagating sound wave back to the transducer. The image is formed by using these reflected pressure waves- if a large portion of the signal is reflected, a brighter (more echogenic) area will be produced at the point of reflection. If no reflection occurs such as within a cyst filled with water, the image will be black [3].

3.2 Resolution and the Fundamental Diffraction Limit

In US, resolution is defined as the ability to discriminate between two different point sources in an image. Resolution can be split into two types: axial resolution refers to the ability to differentiate two points that are parallel to the US beam (along the longitudinal depth axis). The axial resolution is proportional to the wavelength of the transducer and the number of cycles transmitted, given by equation (1):

$$dz = \frac{\lambda N}{2} \tag{1}$$

where λ is the wavelength corresponding to the transducer and N is the number of cycles transmitted. The second definition of resolution is the lateral resolution, or the ability to resolve two objects perpendicular to the US beam. The lateral resolution is proportional to the wavelength, transducer aperture (the width of all the piezoelectric elements in the transducer combined), and depth of the objects. The lateral resolution is defined as the full width at half max in equation (2):

$$dx = \frac{1.206\lambda z}{D} \tag{2}$$

where λ is the frequency, z is the depth of the object, and D is the size of the transducer aperture. The lateral resolution may be called the full-width-half-max (FWHM). FWHM defines the width of the parabolic intensity profile of the ultrasound beam at half the maximum value. FWHM increases as a function of depth, meaning that the lateral resolution worsens as the objects to be imaged are further from the transducer on the depth axis. When the size of an object is significantly smaller than the spatial resolution defined by the system, the object will appear as a spot with axial and lateral dimensions defined by the equations in (1) and (2). This spot is called the point spread function of the system, and is estimated as a two dimensional gaussian [4].

3.3 Plane-wave and coherent compounding

In conventional US imaging, a typical image is reconstructed using multiple scan lines. Each scan line is obtained by transmitting a focused pulse to a certain location in the tissue, and then receiving all scattered and reflected echos. The next scan line is focused to a slightly shifted location, and the process is repeated until an entire image is formed. In this method of US imaging the maximal frame rate is limited as described in the following equation:

$$f_R = \frac{1}{T_{frame}} = \frac{1}{t_{line} * N} = \frac{1}{\frac{N * 2 * Z_{max}}{c}} \tag{3}$$

where N is the number of lines, Z_{max} is the maximal reconstructed depth, and c is the speed of sound [4]. This method of imaging limits the temporal resolution.

Plane wave (PW) imaging is used to increase the maximal frame rate and acquisition time of an image. In PW imaging, all elements are used simultaneously in both the transmission and

reception of the US wave- pulses are not focused upon transmission. In this case, the maximal frame rate achieved is limited only by the imaging depth Z_{max} and the speed of sound *c*:

$$f_R = \frac{c}{Z_{max}} \tag{4}$$

Although the maximal frame rate is increased, PW imaging has a significantly lower resolution than is obtained by scanning focused lines. Coherent compounding is a beamforming method used to improve the resolution of PW imaging. In this technique, a number of PWs are transmitted at different angles to form a single frame [13]. All elements in the transducer are used for each transmit and receive event. The echoes scattered from the tissue at each angle are combined by summing the phase-aligned RF signals, as demonstrated in figure 1 [14]. The resulting image has improved resolution while still achieving ultra-fast frame rates.

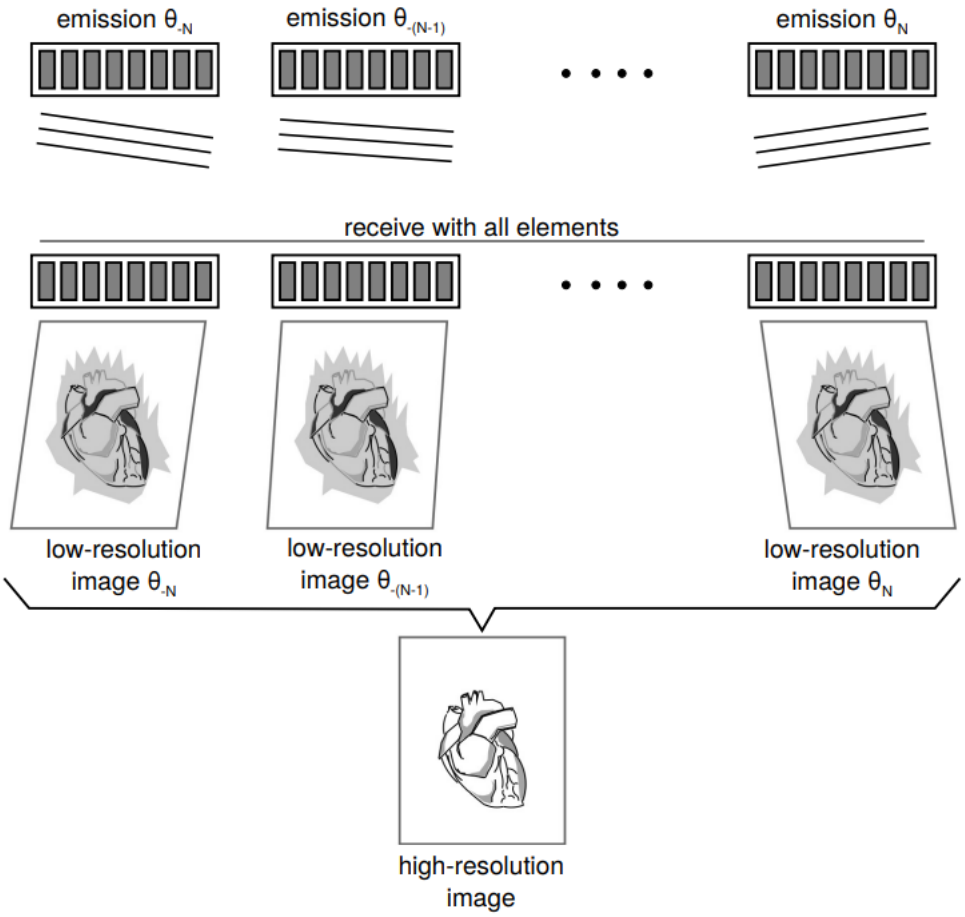

Figure 1. Coherent compounding beamforming illustration. Transmitting N angled plane waves creates N low-resolution images. The combination of these N phase-aligned RF signals results in a high-resolution image. Reprinted from Jensen, Jonas. "Fast plane wave imaging." Ph. D. dissertation (2017).

3.4 Harmonic Imaging

The propagation of a US wave through a tissue is generally assumed to be linear. In reality, some tissues display non-linear behaviors- the amplitude of a signal at a location in the tissue is not proportional to the input excitation. MB contrast agents also behave non-linearly. The impact of non-linearity on the transmitted US wave results in the generation of harmonic frequencies in the signal due to beam distortion and pulse accumulation. In harmonic imaging, an image is formed by detecting these harmonic frequencies [4]. In the simplest approach, a bandpass filter may be used to keep only the harmonic frequencies while leaving out the center

frequency. In this study, we utilized a more advanced contrast pulse sequence (CPS) imaging protocol to differentiate the non-linear MB contrast agents from the relatively linear tissue and phantoms used. In CPS a series of three subsequent transmissions is used; the first short pulse is transmitted with a positive amplitude of 0.5, followed by a pulse with inverted phase and an amplitude of 1, and then another half amplitude pulse with a positive amplitude of 0.5, as illustrated in figure 2. When the resulting wave propagates through a linear medium, such as agar, gelatin, or water- the summation of the backscattered echoes is near-zero [15]. When the waves reach a non-linear medium or scatterer, such as a MB, the summation of the backscattered echoes is retained.

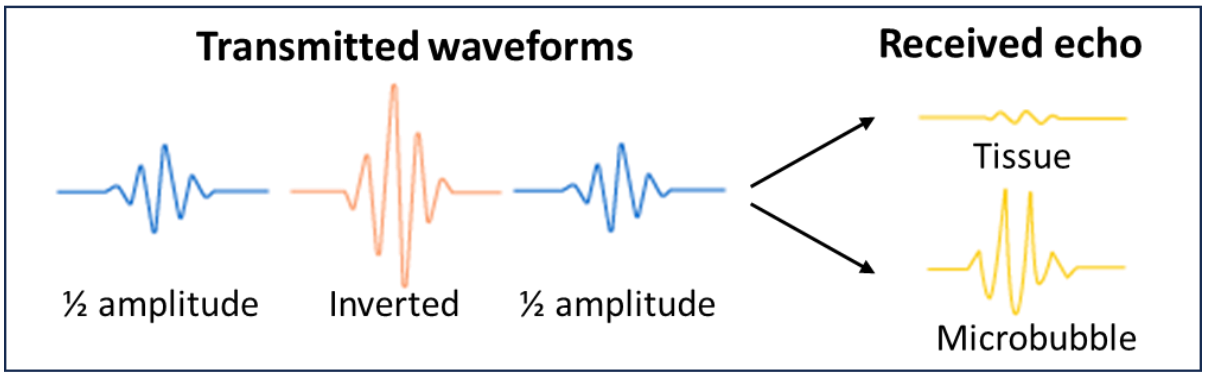

Figure 2. Illustration depicting the transmitted waveforms and resulting received echoes in CPS imaging, resulting in a strong echo from non-linear microbubbles and a negligible echo from linearly behaving tissues.

3.5 Safety in ultrasound imaging

Medical imaging using US is considered one of the safest imaging modalities. When imaging, the US wave interacts with biological tissue. Exposure to US waves is generally considered non-invasive, however, there are mechanisms that may cause biological effects in tissues when interacting with an US wave. The first mechanism is due to thermal effects- energy from the US wave is partially absorbed in the tissue, which leads to a rise in temperature. The significance of heating within a tissue depends on the duration and the magnitude of the

temperature rise itself. Higher temperatures require less time to produce biological effects within the tissue. Non-thermal effects, or mechanical effects, are the second mechanism that may cause damage to biological tissues in US imaging. The US pressure wave has a negative portion, which can remove gas from the tissues. This may cause gas bubbles that grow, expand, and contract in response to the US wave. High pressures and temperatures may lead to the collapse of these gas bubbles or microstreaming in fluids. These effects are highly unlikely to occur in diagnostic US imaging [16].

To assess safety in US imaging procedures and predict the possibility of undesirable effects two metrics were defined. The thermal index (TIS) for soft tissues is defined as the ratio of the transmitted acoustic power- usually a parameter determined by the user during the scan itself- to the power required to raise the temperature of a tissue by 1°C. According to FDA regulations the TIS must be under 6 for all applications other than ophthalmology, in which the *TIS* must be under 1 [17]. The *TIS* is defined by equation (5):

$$TIS = \frac{W_0 \times f}{210mW \times MHz} \tag{5}$$

Where f is the transmitted frequency of the wave in MHz and W_0 is the power applied in mW.

The possibility for mechanical bio-effects is determined using the mechanical index (MI). In US imaging applications, the *MI* is limited to below 1.9 by FDA regulations [18].

$$MI = \frac{PNP}{\sqrt{f}} \tag{6}$$

where the *PNP* is the peak negative pressure of the wave and is given in MPa, and f is the frequency of the transmitted wave given in MHz.

3.6 Microvasculature Blood Flow

Microvascular circulation within the body has many important functions, including metabolic transfer processes between the blood and cells, the regulation of blood pressure, and the regulation of temperature. Clinically, research in this field may aid in assessment of many conditions that are affected by microvascular blood flow throughout the body, such as benign and malignant lesions, diabetes, and retinopathy [19]. The understanding of blood flow within the body must include the ability to study blood vessels ranging from 2 μm – 200 mm and blood flows ranging from 30 cm/sec in the aorta to 0.026 cm/sec in the capillaries [20].

There are a multitude of methods used to study and image microvascular blood flow within the body. Each method has limitations in terms of maximal imaging resolution, penetration depth, and acquisition time [21]. Doppler ultrasound can be used to calculate blood flow at a large penetration depth; however it is limited both in spatial resolution and the ability to measure both low and high blood velocities [22]. Near-infrared II fluorescence has a high spatial resolution of 30 μm and temporal resolution of less than 200 ms per frame, but is limited to an imaging depth of 1-33 mm [23]. Micro-computed tomography and magnetic resonance imaging (MRI) have deep tissue penetration and high spatial resolution, however they require long scanning times that can take upwards of one hour [24]. Ultrasound localization microscopy (ULM), described in detail in 3.7, has many advantages in imaging both microvascular network structures and blood flow.

3.7 Ultrasound Localization Microscopy

ULM is an ultrasound imaging technique used to overcome the diffraction limit and image micro-vascular flow deep within tissues. In ULM, a low concentration of MBs is injected into the blood stream where they are individually localized and tracked over thousands of frames.

MBs are significantly smaller than the resolution limits of the US system, therefore each MB appears as the PSF of the ultrasound system. In most implementations of ULM, it is assumed that the MB concentration in the blood is low enough that the individual PSFs are separable. The center of each individual PSF is localized at a sub-pixel resolution using one of many methods such as the weighted average, gaussian-fitting, or radial symmetry of the neighboring pixels surrounding a possible MB center [25]. The localized MBs are tracked through consecutive frames, most often by using a nearest-neighbor approach but other methods such as Kalman filtering are also widely used. The localizations and tracks are up sampled by up to 10-times the original size, and then used to form a density image of the localizations and a velocity map using the calculated velocity of each track. The summation of localizations over thousands of frames forms the final super-resolved image. The individual tracks are converted into velocity using the known frame rate and the corresponding size of a pixel, and then averaged over time to form the velocity map which captures velocities ranging from 0.1-10 mm/sec and even more given that the MBs are sparse [26]

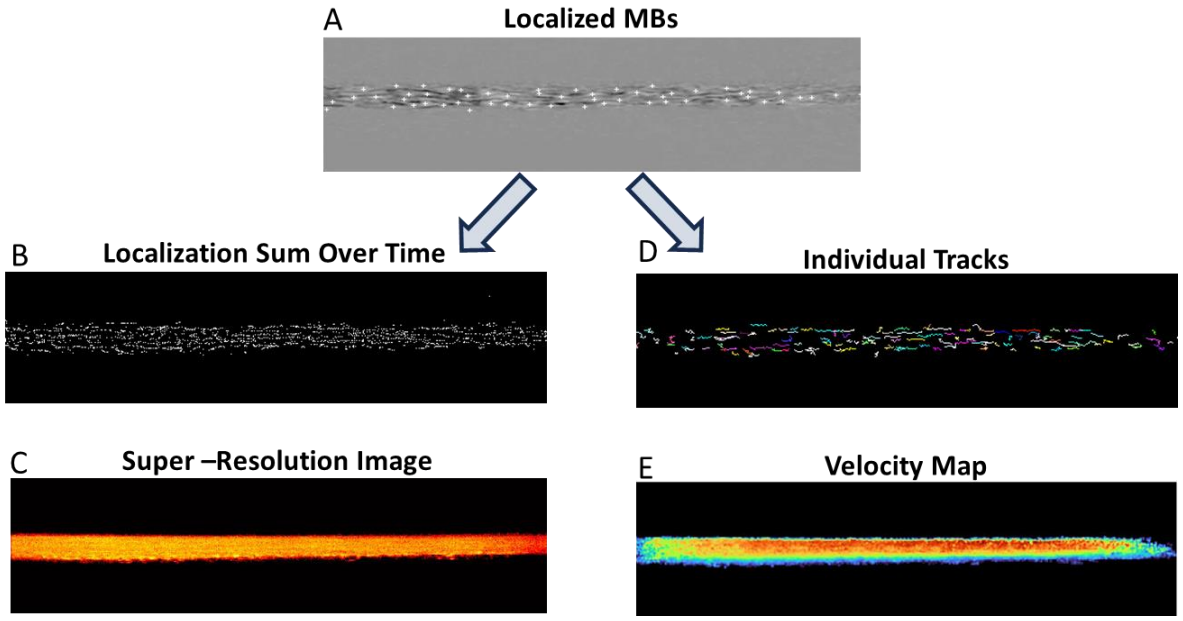

Figure 3. Illustration of the ULM process. (A) The MBs are localized at a sub-pixel accuracy in each US frame. (B) Localizations from each frame are summed over time. (C) The summed localizations form the final super-resolution image. (D) The localized MBs are tracked throughout consecutive frames to form individual tracks. (E) The velocity represented by each individual track is calculated and averaged over all tracks to form a final velocity map

ULM is most often implemented at ultrafast frame rates that can range from 100-1500 frames per second. This is achieved by utilizing plane wave imaging and coherent compounding, as described previously. Ultrafast frame rates allow for more accurate tracking of MBs because MBs move minimally between frames, making tracking a straightforward nearest-neighbor calculation between consecutive frames. Additionally, in order to help differentiate between MB signal and tissue signal in vivo- contrast pulse sequences may be used to further enhance to MB signal and reduce echoes produced by tissues [26]. In its most basic form the time needed to acquire data for a full super-resolution image using ULM is a factor of the number of frames and the frame rate, but may also need to account for frames that are not used due to large motion artifacts caused by breathing [27]. The number of frames acquired ranges from 40,000-100,000 in various studies, and total acquisition times can range from under a minute to upwards of 10 minutes [28].

Tracking of MBs at high frame rates through micro-vessels allows to reconstruct super resolved images and velocity maps of vascular structures as small as 5 μm, an order of magnitude below the diffraction limit [7], [25], [26]. ULM can be used to track average blood velocities ranging from under 1 mm/sec to several cm/sec, and to track flow oscillations in functional brain neurovascular activity [29]. ULM has been demonstrated in simulations, tissue-mimicking phantoms, and in-vivo in different organs such as rat brains [28], [30] and kidneys [25], [27]. In vivo ULM is limited in the ability to compare different conditions and perform repetitive imaging of identical vascular networks for statistical purposes. In addition, the ground-truth vessel sizes, flow rate, and full configuration of the network is generally not known. It is known that MBs

behave and oscillate differently in different sized vessels [31], [32]. The field of ULM imaging is rapidly expanding, with developments occurring in all stages from data acquisition to the post-processing localization and tracking of MBs. Therefore, the creation of a blood vessel mimicking phantom for ULM is of great interest.

3.8 Singular value decomposition filtering

SVD filtering is a technique used to filter multi-image US data acquired over time. A single ULM acquisition consists of a stack of thousands of beamformed US images over the course of seconds to minutes. SVD filtering can be used to filter this stack of images by removing the static tissue signal, the gaussian noise, or both. It is assumed that the acquisition consists of three main components- the clutter signal produced by tissues, the blood signal which contains flowing MBs, and electronic or thermal noise (which can be considered a zero-mean Gaussian white noise). Each component has different spatiotemporal characteristics. The signal returning from areas in which MBs are flowing through blood or liquid has a high temporal frequency, whereas tissue or relatively stationary areas display a low frequency. In parts of the acquisition where there is no blood flow over time, a pixel may exhibit slight fluctuations due to movements such as heartbeats or breathing. Conversely, in regions with blood flow, a pixel will display significant fluctuations caused by the motion of MBs and blood cells. Furthermore, the blood flow signal lacks high spatial coherence when compared to the tissue signal. To differentiate between these two signals, the singular value decomposition of the raw ULM data can be employed [33].

The spatiotemporal stack of raw US data can be denoted by $n_x \times n_z \times n_t$ samples- the number of spatial samples along the x- direction, the z-direction, and the number of time samples (corresponding to the number of frames in the acquisition). The raw data is reshaped into a

Casorati matrix by transforming the original stack of images into a 2D space-time matrix with dimensions $n_x \times n_z, n_t$ as displayed in figure 4 [34].

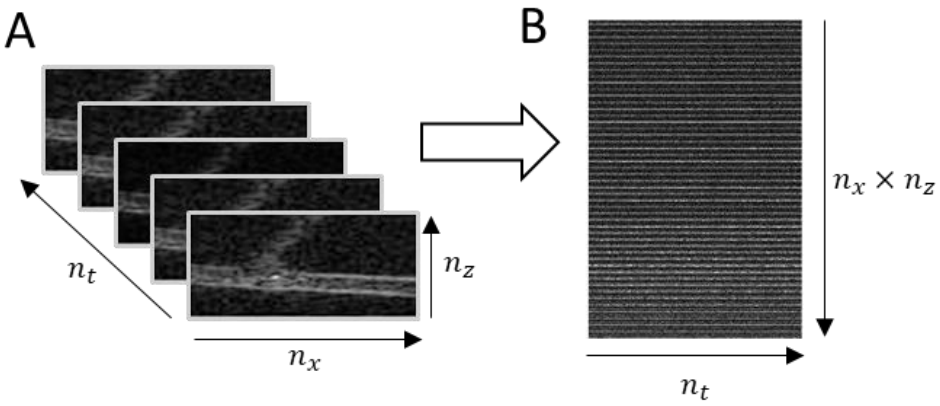

Figure 4. Casorati matrix. (A) a stack of n_t US images, with each image having the dimension of n_x, n_z. (B) The reconstructed Casorati matrix of dimensions $n_t, n_x \times n_z$. Each row of the matrix consists of a single pixel location in the stack of images over time.

Singular value decomposition is performed on the Casorati matrix (denoted as **S**), which consists of finding three matrices such that:

$$\mathbf{S} = \mathbf{U\Delta V}$$

Where **Δ** is a non-square diagonal matrix and **U** and **V** are orthonormal matrices. The columns of **U** and **V** correspond to the spatial (**U**) and temporal (**V**) singular vectors of the matrix **S**. The diagonal matrix **Δ** consists of the corresponding singular values. SVD filtering is achieved by zeroing-out the first singular values which equates to the removal of static areas and slow tissue motion [33].

Although this study consists mainly of data acquired from a phantom, we found that it was difficult to remove the strong echo received from the walls of the channel within the phantom. MB localization algorithms are based on adaptive filtering or finding the brightest points in each image, and therefore having a strong constant signal resulting from the channel

wall is undesirable. SVD filtering was implemented to remove the strong echo and extract only the flowing MB signals.

3.9 Tissue Mimicking Phantoms

Significant challenges exist in engineering complex tissue-mimicking vascular phantoms for ultrasound imaging applications. Due to their complexity, most ULM phantoms rely on single channels. The single channel can be placed within a water tank, however the vessel boundaries reproduce a strong echo that obscures the MB signal and needs to be filtered out. Alternatively, the channel can be created by embedding a tube within an agarose or gelatin-based mold, and after solidifying, the tube is pulled out and an empty channel is formed. Although useful, this technique is suitable mostly for single wide channels. Channels smaller than 200 μm are difficult to fabricate and handle, due to the need to inject the MB suspension into the channel. Nevertheless, elaborate flow phantoms that contain branching channels are vital to the study of flow patterns using ultrasound. In ultrasound imaging, an X shape phantom was created by crossing two single channels, however since the channels were located one on top of the other, they are inherently unaligned in the elevation plane [28]. A custom 3D printer was also developed for the creation of ultrasound flow phantoms, yet it is a costly solution that created vessels with diameters of 200 μm [35], [36]. In a recent study, wire templating was used to create branching vessels in hydrogels with diameters under 50 μm that are compatible with US imaging. However, this study did not gain full control over the final thickness of the vessels and cannot create vessels that merge back together. Additionally, the method is relatively complex and does not allow to consistently reproduce identical phantoms [37]. Microfluidic devices are yet another alternative that is a well-established platform for the study of flow using optical imaging. Recently, such devices were used to image MB oscillations following ultrasound excitation [38]. These devices

are typically composed of polymeric materials such as polydimethylsiloxane (PDMS), that highly attenuates ultrasound. Therefore, the use of microfluidic devices for ULM is limited due to the weak signal that echoes from isolated MBs. Soft tissues such as fat, breast, kidney, and liver have an acoustic impedance which ranges from 1.4-1.7x10^6 kg/m^2 and an attenuation coefficient of 0.48-1 dB/cm/MHz. PDMS and other elastomers do not mimic the acoustic properties of biological tissue- for example, PDMS has an acoustic impedance of 1.1x10^6 kg/m^2 and an attenuation coefficient of 3-20 dB/cm when measured at frequencies ranging from 1 to 6 MHz. This emphasizes the importance of finding a hydrogel based solution. A 10% gelatin solution, as used in this study, has an acoustic impedance of 1.55 x10^6 kg/m^2 and an attenuation coefficient of approximately 0.5 dB/cm/MHz, falling within the range of biological tissues commonly imaged using ultrasound [39]. Many additional phantom studies performed using hydrogels were limited in vessel size and complexity [7], [30], [40], [41].

3.10 Proposed method concept

Our aim was to develop a new class of ULM phantoms that contain complex blood-vessel mimicking channels with full control over bifurcating vessels thickness, angle, and length, to provide a manner to study ULM in a controlled environment and serve as a perquisite step prior to in vivo experiments. We fabricated a gelatin-based phantom using a two-part machined mold with one side consisting of the negative of the planned vessel network, with rods to create inlets and outlets for controlled flow. Gelatin is an ultrasound compatible material, with minimal attenuation that mimics that of soft tissues within the human body. In addition, it fully cross-links after congelation. Therefore, the two parts were extracted and combined when the gelatin partially congealed, and the gelatin fully congealed in the final assembly, to yield a one-piece bonded ULM phantom. This phantom was used here to study the physical properties of MB flow

and distribution using ULM to mimic results that have been displayed in-vivo in situations where the ground truth is unknown. First, we characterized saturation time as a function of microbubble concentration. Next, we reconstructed velocity maps of phantoms with bifurcation angles of 25° - 55° at flow rates from 0.01-0.03 ml/min and explored the effect of bifurcation angle and flow rate on acquisition time. We then explored acquisition time to full saturation of phantoms with vessel widths ranging from 500 – 100 µm. Lastly, to demonstrate the robustness of the phantom fabrication method, we created two additional phantoms- one with a trifurcation with angles of 30°, with one inlet and three outlets. We then created a phantom with a trifurcation with angles of 30° in which the channels branch out and then converge into a single outlet that mimics many commonly seen microfluidic devices. The method is summarized in figure 5.

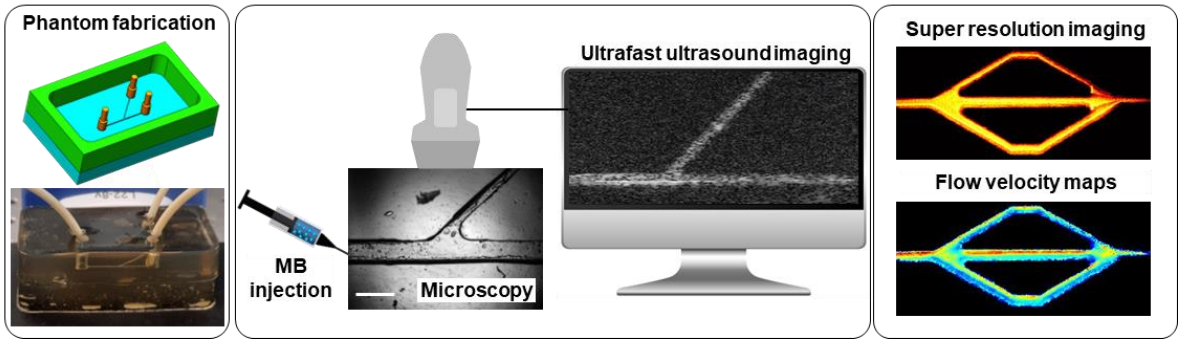

Figure 5. Proposed method concept illustration. A two part-gelatin phantom is created using a CNC machined aluminum mold. A diluted MB solution is injected using a programmable flow machine and imaged at ultrafast frame rates. The acquired data is used to produce super resolution images and flow velocity maps. Scale bar is 1 mm.

A future goal is to use these phantoms to test flow and saturation time differences between different contrast agents in a controlled environment by comparing MBs and significantly smaller NBs. We conducted preliminary experiments which display a difference in saturation time of the smaller branching channel of the phantom with a 300 µm main channel and 100 µm branching time when comparing MBs to NBs.

4 Materials and Methods

4.1 Microvessel Phantom Fabrication

The process used to fabricate gelatin phantoms with branching microfluidic channels is shown in Fig. 6. The method is inspired by techniques used in tissue-engineering studies [42], [43]. A two-part aluminum mold was fabricated by a computerized numerical control (CNC) machine. Each part consisted of a base and walls connected by screws. The base of the first part consisted of a protruded negative of the desired microfluidic channel, with attached rods that will create inlets to the phantom. The second base was smooth (Fig. 6A). The process allowed full control over the main and branching vessels thicknesses, and the bifurcation angle. Gelatin powder (G9382, Sigma-Aldrich) was mixed with deionized water to a 10% solution at ambient temperature and heated until all powder was completely dissolved. The solution was then poured into the molds and allowed to cool for 2 hours at room temperature (Fig. 6B). The partially cross-linked gelatin was then demolded by unscrewing the walls from the base and extracting the gelatin from the base, carefully assembled together, with the channel positioned in the middle of the assembly and placed at 4° C for 6 hours to fully crosslink.

Seven different phantom configurations were created. Each had a different base that corresponded to the desired branching pattern. All the phantoms consisted of a main channel and a branching channel that split off from the main channel. All configurations had a rectangular cross-section with a channel height of 300 μm and a total channel length of 20 mm, which is larger than the maximal field of view of the transducer. The bifurcating phantoms consisted of a main channel and a branching channel that split off from the main channel. The first set of three phantoms consisted of channel widths of 300 μm with branching channels at 25°, 45°, and 55° angles. A fourth configuration had a main channel width of 500 μm and a branching channel

width of 200 µm, with a 45° bifurcation. The final phantom configuration had a main channel width of 300 µm and a branching channel width of 100 µm, with a 45° bifurcation. The two additional phantoms consisted of trifurcating channels at angles of 30° with 300 µm channel widths. The first included a main channel that split into three equally sized channels which each reach a separate outlet. In the second, the channel split into three equally sized channels and then converged back into one channel, similarly to classical microfluidic chips. Prior to each experiment the phantom inlets were connected with tubing to a 2.5 ml syringe filled with diluted MB solution. The syringe was placed on a programmable flow inducing pump (GenieTouch, Kent Scientific, Torrington, USA) set at flow rates of 0.01, 0.02, and 0.03 ml/min. The flow rates in the various phantoms span a velocity range of 1-17 mm/sec, covering the span of velocities detected by ULM in-vivo studies [28]. A custom-made 3D printed case was created for the US transducer and screwed into an optic table to ensure the transducer is held parallel to the channels within the phantom and at the correct elevation to acquire the maximal signal (Fig. 6 D).

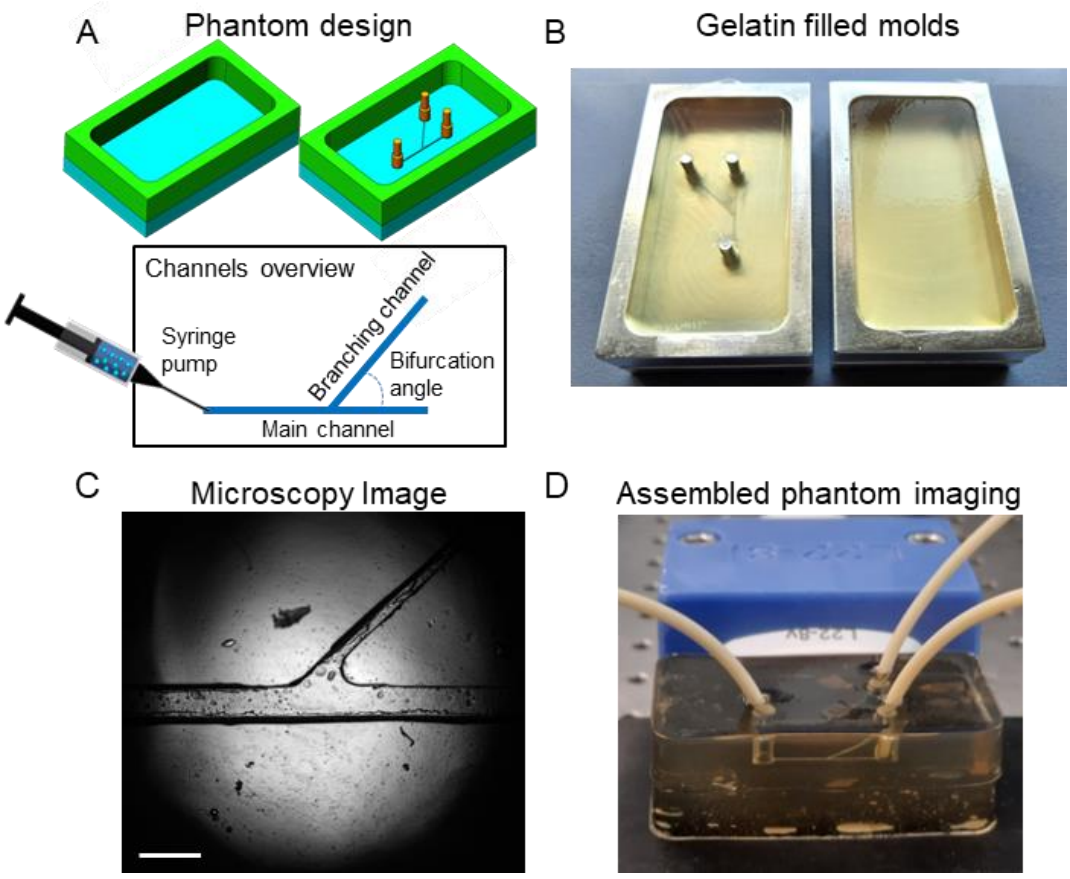

Figure 6. Microvessel phantom fabrication. (A) Schematic illustration of the two part mold and overview of the network. (B) Gelatin poured into aluminum molds. (C) Microscopic image of the gelatin-based channels, scale bar is 1 mm. (D) Assembled phantom with tubing connected to inlets and outlets, imaged with an L22-8v transducer.

4.2 Bubble Preparation

MBs were composed of a phospholipid shell and a perfluorobutane (C4F10) gas core, and prepared as reported in previous studies[44]–[46]. Briefly, DSPC and DSPE-PEG2K were dissolved into propylene glycol by heating and sonicating at 62° C until the lipid powders were completely dissolved. This was added to a mixture of glycerol and phosphate buffer solution that was preheated to 62°. The resulting solution was sonication for 10 min at room temperature and then 1mL of solution was transferred into a 3mL headspace vile and saturated with C4F10 gas before sealing. Before use, the MB vials were shaken for 45 seconds in a vial shaker and purified via centrifugation to remove MBs with radii smaller than 0.5 µm. Size selection was performed

using centrifugation to remove MBs with a diameter larger than 5 μm. The size and concentration of MBs were measured using a particle counter system (Accusizer FXNano, Particle Sizing Systems, Entegris, MA, USA). The MBs were used within 3 h of their preparation. The size distribution and concentration varied by less than 10% between measurements. The MBs were diluted with phosphate buffer saline in a 2.5 ml syringe to concentrations of 1.6x106, 6.4x106, and 6.4x107 MBs/ml to test acquisition time to full saturation as a function of MB concentration. For all other experiments, MBs were diluted to 6.4x106 MBs/ml.

NBs were composed of 1,2-dibehenoyl-sn-glycero-3-phosphocholine (C22), 1,2-dipalmitoyl-sn-glycero-3-phosphate (DPPA), 1,2-dipalmitoyl-sn-glycero-3-phosphoethanolamine (DPPE), and 1,2-distearoyl-sn-glycero-3-phosphoethanolamine-N-[methoxy(polyethylene glycol)-2000] (ammonium salt) (DSPE-mPEG 2000) (Sigma-Aldrich) dissolved into propylene glycol by heating and sonicating to 80°C. Glycerol and PBS were mixed and preheated to 80°C and added to the lipid solution. The resulting mixture was sonicated at room temperature for 10 minutes, and then 1mL of solution was transferred into a 3mL headspace vile and saturated with C3F8 gas before sealing. Before use, a vial was activated by mechanical shaking for 45 s in a Vialmix shaker. The vial was placed inverted into a centrifuge and then centrifuged at 50 rcf for 5 min.

4.3 Ultrasound acquisition

A high frequency transducer L22-8 (Kolo Medical, USA) controlled by a programmable ultrasound system (Vantage 256, Verasonics, WA, USA) was used for ultrafast imaging of MBs, using a custom contrast pulse sequence (CPS) written using MATLAB (version 2020a, MathWorks, Natick, MA, USA). A center frequency of 10 MHz was transmitted and the second harmonic frequency of 20 MHz was received, both within the bandwidth of the transducer.

Imaging was performed at a mechanical index (MI) of 0.14. The MI, a parameter that determines the likelihood of creating mechanical damage within the tissue as a result of US application, is defined as the peak negative pressure (PNP) divided by the square root of frequency. For imaging applications, the food and drug administration (FDA) limits the MI to a value below 1.9 [18]. The MI was calibrated using a needle hydrophone (NH0200, Precision Acoustics, UK) in a degassed water tank. Frames were coherently compounded with angles at -5°, 0°, and +5°, where at each angle three successive pressure waves were transmitted using a CPS with a summed overall amplitude of zero (0.5, -1, 0.5) to take advantage of non-linear scattering response of MBs and reduce the response of linear scatters [15]. Data was recorded in continuous 1500 frame blocks at a frame rate of 250 Hz. Velocity maps were reconstructed using a total of 9000 frames, and saturation curves were calculated over 3000 frames. MB concentration and vessel width experiments were performed at a flow rate of 0.02 ml/min.

4.4 ULM Image Processing and Data Processing

The ULM algorithm consisted of up-sampling and interpolating each original frame to 2x the original using the pre-trained Fast Super-Resolution Convolutional Neural Network (FSRCNN) [47]. Next, MB signals were enhanced using singular value decomposition filtered by removing the first two singular values [33] and applying a second order Butterworth high pass filter. Peak detection and localization were performed using adaptive filtering, extraction of the brightest points in the image, and calculating a weighted average on neighboring pixel intensities at each point. After SVD and adaptive filtering, it is assumed that the brightest points in the image are MBs and not noise or the channel walls. The sub-pixel center of each MB is determined using the weighted average of the neighboring pixels that correspond to the PSF of the system. Localized PSFs tracking was achieved by calculating minimum-distance between PSFs in

consecutive frames, and velocity was computed as the displacement between consecutive frames at a known frame rate. For image rendering purposes, the individual tracks were interpolated to close gaps between consecutive localizations- creating a smoother final image that represents the physical flow of MBs. For all other purposes such as time to saturation calculations, the raw data localizations were used. Only MBs that could be tracked for over 10 consecutive frames were included in the final velocity calculations in order to avoid adding incorrect tracks.

Expected velocity within channels was calculated using Euler's simplified conservation of mass with known cross sections and a known flow rate at the input of the phantom, according to:

$$\mathbf{A_{in}V_{in} = A^{1}_{out}V^{1}_{out} + A^{2}_{out}V^{2}_{out}} \quad (1)$$

where A is the area of the rectangular cross-section and V is the velocity within the channel of the flow at the input and outputs of the phantom. In the phantom with equal channel cross-sections for the main and branching channels, $Vout^1 = Vout^2$ from symmetry.

The experimental velocity profiles were calculated by averaging 10 consecutive profiles perpendicular to the direction of flow in the channel immediately before and after the bifurcations. This was to ensure that the displayed profiles are unbiased and accurately represent the average flow calculated within the channels.

Saturation time curves were created by setting a range of interest (ROI) of 25x25 pixels immediately after or before the bifurcation in a super-resolved image. The localizations of MBs within the channel starting at time 0 until full saturation of the channel were then observed. Full saturation occurs when a MB localization event occurred in all the pixels within the vessel passing through the ROI. The curves were normalized by their maximal value and fit to an exponential function to calculate the time to 63% of full saturation, defined as τ. Statistical analyses were performed using Prism9 software (GraphPad Software Inc.). Results are presented

as mean ± SD. Statistical tests are reported in the relevant captions. P values less than 0.05 were considered significant.

4.5 In Vivo Data Processing

In vivo data consisting of 40,000 frames of MBs flowing through a rat kidney was acquired from previous studies, and analyzed as suggested in [27]. The data was acquired at a frame rate of 300 Hz using a CPS pulse sequence. Cardiac and respiratory induced motion was estimated by calculating cross-correlation between successive frames. When there is movement between successive frames, there is a drop in cross-correlation. When there is little movement between successive frames, the cross-correlation remains closer to 1. Cardiac motion causes a repetitive pattern with a small drop in cross-correlation corresponding to the heart rate of the animal. Respiratory related motion causes significant shifts in the field of view where the cross-correlation drops drastically, and therefore these frames were removed from data analysis. The removed frames are marked as respiratory motion between the dotted red lines (Fig. 7). The remaining data was then processed using the ULM algorithm described previously, and saturation time curves were calculated for two vessels in the kidney- one larger vessel, and one smaller one.

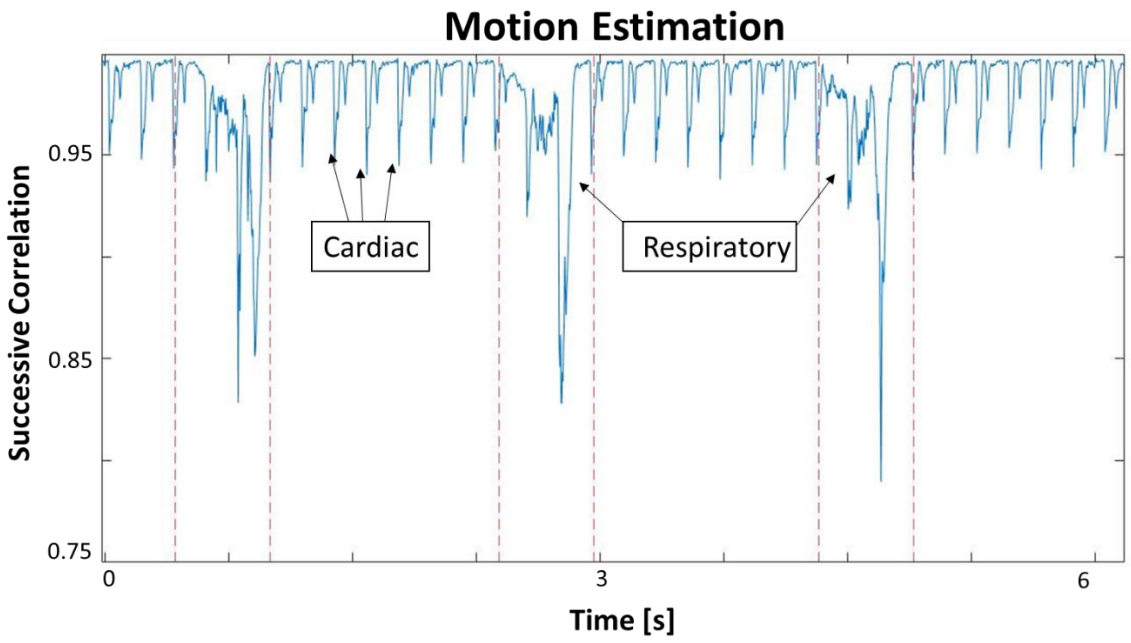

Figure 7. Motion estimation and classification. The cross correlation indicates the small changes in the position of the kidney due to cardiac movement and the larger changes due to respiration, which cause a large drop in correlation.

5 Results

5.1 MB Concentration Optimization Results

Initial experiments were performed using a 300 µm vessel that branched into two channels of 300 µm at a splitting angle of 45°. First, the optimal MB concentration for phantom imaging was identified by assessing the image saturation curve over time for three MB concentrations (Fig. 8). Saturation was calculated in a 25x25 pixel range immediately after the bifurcation (Fig. 8A). Full saturation was achieved when localized MB events were detected in each pixel within the vessel passing through the window (white rectangle, Fig. 8A). The characteristic time to 63% saturation (τ) was calculated for each curve fitted to an exponential function. The lowest concentration evaluated, 1.6×10^6 MBs/ml, yielded significantly longer times to saturation of the branching channel. The low concentration (1.6×10^6 MB/ml) τ value of 2.15 ± 0.85 sec was found

to be significantly lower ($p<0.05$) than both the high and medium concentration values. The medium concentration ($6.4x10^6$ MB/ml) and high concentration ($6.4x10^7$ MB/ml) yielded similar τ values of 0.94 ± 0.23 sec and 0.83 ± 0.25, respectively ($p>0.05$, Fig. 2). These values are summarized in Table 1. The high MB concentration was such that individual MBs were overlapping, which lowered the MB tracking accuracy and affected the final super-resolved images. The medium concentration of $6.4x10^6$ MB/ml yielded an optimal saturation time without compromising the algorithm's tracking accuracy and hence was used in all following experiments.

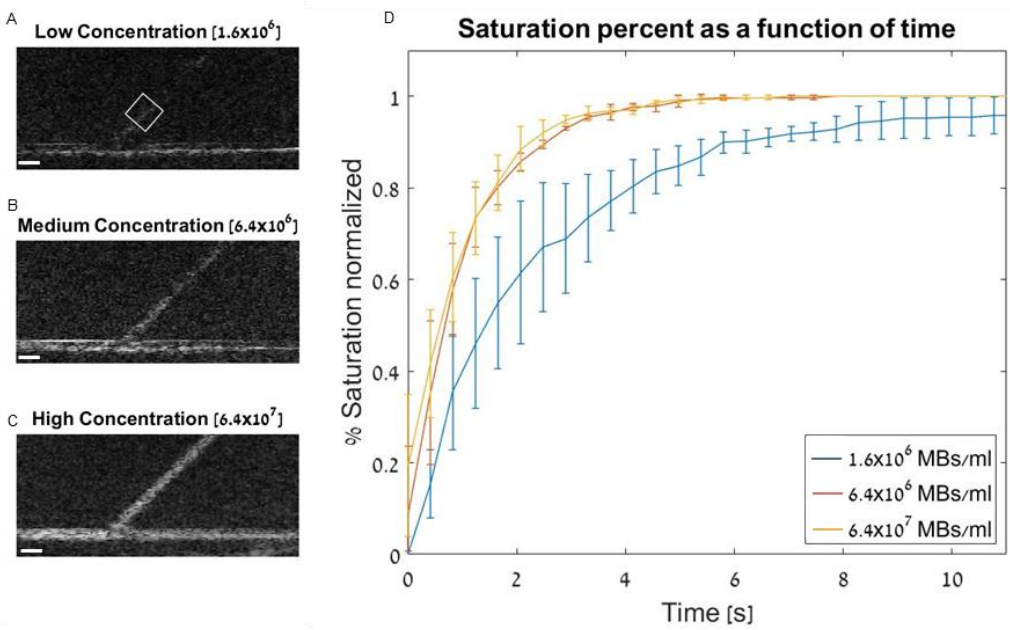

Figure 8. MB concentration optimization in a bifurcating vessel phantom with channel diameter and height of 300 µm and a bifurcation angle of 45°. (A-C) Representative images from each MB concentration dataset, including a white rectangle 25x25 pixel ROI used for all calculations. All scale bars are 1 mm. MB concentration: (A) $1.6x10^6$ MBs/ml; (B) $6.4x10^6$ MBs/ml; (C) $6.4x10^7$ MBs/ml. (D) Normalized saturation percent of the ROI over time for the three MB concentrations. $R^2 > 0.98$ for all fit curves used to calculate τ. All experiments were performed in triplicate, and all data are plotted as mean ± SD.

Concentration	τ value [sec]
Low	2.15 ± 0.85
Medium	0.94 ± 0.23
High	0.83 ± 0.25

Table 1. Summary of saturation times for MB concentration optimization.

5.2 Velocity estimation as a function of bifurcation angle

The effect of bifurcation angle and velocity on full channel saturation time was evaluated next. In these phantoms both the main and branched channels had a diameter of 300 µm, while the branching angle was either 25º, 45º or 55º. Flow velocity profiles were detected by tracking the flowing MBs in the microfluidic inspired phantoms for three flow velocities of 0.01, 0.02 and 0.03 ml/min (Fig. 9). The saturation time curves were calculated for the main and branching

channels to evaluate the effect of bifurcation angle on saturation time of the branching channel vs. the main channel (red and white squares in Fig. 9A). The 55° bifurcation yielded a τ value of 1.84 ± 0.28 sec for the main channel and 2.20 ± 0.30 sec for the branching channel. The 45° bifurcation yielded a τ value of 1.30 ± 0.01 sec for the main channel and 1.62 $\pm$ 0.32 sec for the branching channel. The 25° bifurcation yielded τ value of 1.72 ± 0.18 sec for the main channel and 2.12 $\pm$ 0.52 sec for the branching channel. These values are summarized in Table 2. No significant difference was found for τ values the main and branching channel for the tested bifurcation angles and flow rates ($p > 0.05$).

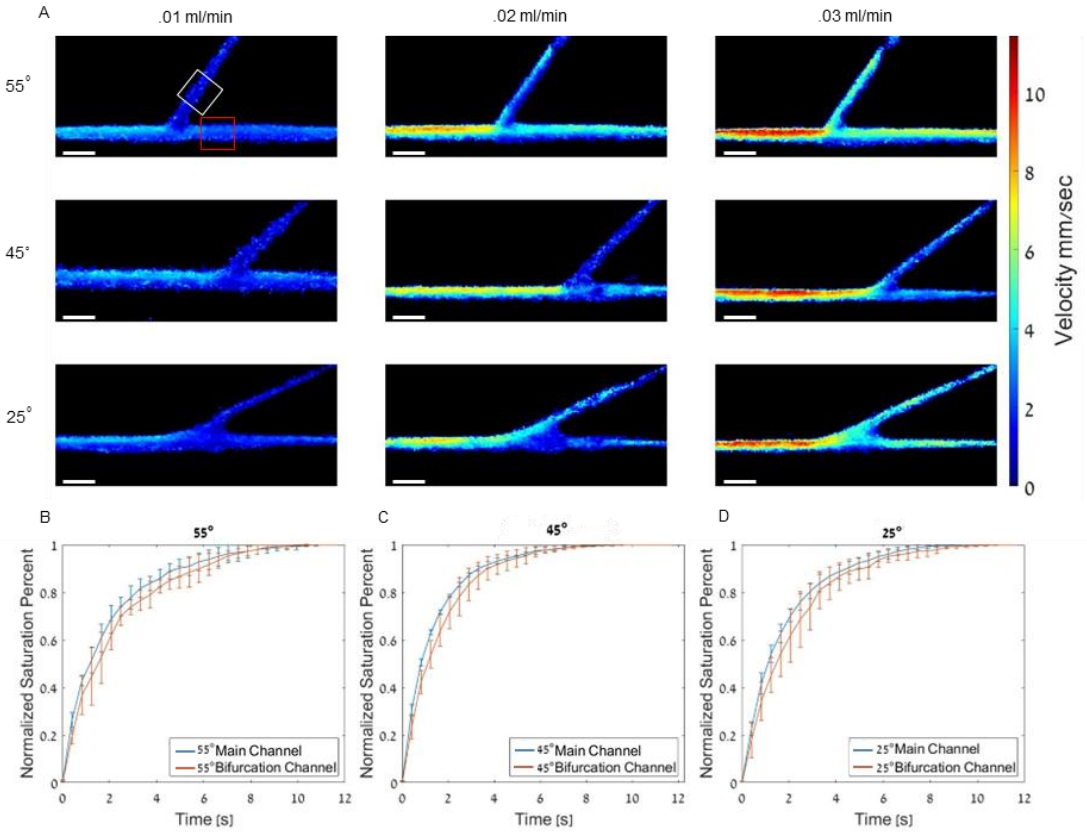

Figure 9. Velocity maps and saturation curves as a function of bifurcation angle**.** (A) Velocity maps of phantoms with bifurcation angles of 55°, 45°, and 25° with flow rates of 0.01, 0.02, and 0.03 ml/min. All scale bars are 1 mm. (B-D) Saturation curve for the main channel and branching channel with bifurcation angle of (B) 55°; (C)

45°; (D) 25° at a flow rate of 0.02 ml/min. P value > 0.05 for all groups. R^2 > 0.98 for all fit curves used to calculate $\boldsymbol{\tau}$. All experiments were performed in triplicate, and all data are plotted as mean ± SD.

Bifurcation angle	τ value main channel [sec]	τ value branching channel [sec]
55°	1.84 ± 0.28	2.20 ± 0.30
45°	1.30 ± 0.01	1.62 ± 0.32
25°	1.72 ± 0.18	2.12 ± 0.52

Table 2. Summary of saturation times as a function of bifurcation angle.

Velocity profiles were calculated for the main channel before the bifurcation, and both the main and branching channel after the bifurcation (Fig. 10). Measured velocity profiles were calculated by averaging 25 successive channel cross sections in the ROI in the white, red, and green boxes (Fig 10A). Expected velocity of the main channel was calculated using the known flow rate and area of the channels, based on Eq. 1. The laminar flow in the channels forms the hyperbolic profiles (Fig 10D-F). Next, the effect of input flow rate on the saturation of the branching channel compared to the main channel after the bifurcation was evaluated (Fig. 10G-I). Saturation time curves of the main and bifurcating channel were compared for each flow rate displayed. At 0.01 ml/min, τ = 1.75 ± 0.30 sec for the main channel and 2.13 ± 1.08 sec for the branching channel. At 0.02 ml/min, τ = 1.84 ± 0.28 sec for the main channel and 2.20 ± 0.30 for the branching channel. At 0.03 ml/min, τ = 1.50 ± 0.20 sec for the main channel and 1.70 ± 0.58 for the branching channel (p > 0.05). These values are summarized in Table 3.

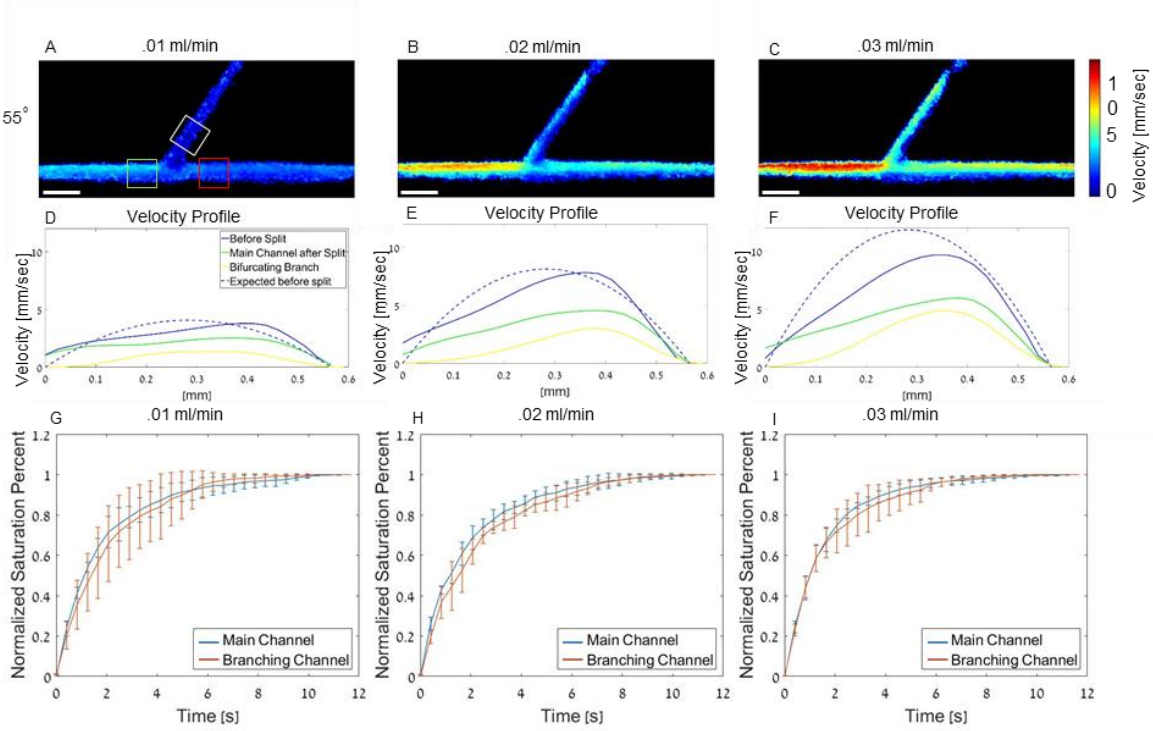

Figure 10. Velocity profiles and saturation curves as a function of flow rate. (A-C) Velocity maps of channels with a 55° bifurcation and flow rates of 0.01, 0.02, and 0.03 ml/min. All scale bars are 1 mm. (D-F) Velocity profiles showing expected velocity of the main channel before the bifurcation, calculated velocity of the main channel before and bifurcation, and of both channels after the bifurcation. (G) Saturation curve for the main and branching channel at 0.01 ml/min. (H) Saturation curve for the main and branching channel at 0.02 ml/min (I) Saturation time curve of the main and branching channel at 0.03 ml/min. No significant difference was found, p value > 0.05 for all flow rates. $R^2 > 0.98$ for all fit curves used to calculate τ. All experiments were performed in triplicate, and all data are plotted as ± SD.

Flow rate [ml/min]	τ value main channel [sec]	τ value branching channel [sec]
0.01	1.75 ± 0.30	2.13 ± 1.08
0.02	1.84 ± 0.28	2.20 ± 0.30
0.03	1.50 ± 0.20	1.70 ± 0.58

Table 3. Summary of saturation times as a function of flow rate.

5.3 Effect of channel widths

The effect of vessel diameter was evaluated. As often occurs in vivo, we focused on assessing the behavior of MBs flowing from a large channel into a smaller channel. The flow rate in all datasets was 0.02 ml/min. Three phantoms were evaluated: 1) main channel of 300 µm and a branching channel of 100 µm; 2) main channel of 500 µm and a branching channel of 200

μm; 3) main channel of 300 μm and a branching channel of 300 μm. Their ULM images are shown in Fig. 11 A-C, respectively. The saturation curves of the 300 μm main channel (τ = 1.21 ± 0.05 sec) and 100 μm branching channel (τ = 2.09 ± 0.33 sec) have significantly different characteristic τ values are when tested with a two-sample t-test (Fig.11D, $p<0.05$). The saturation curves for the 500 μm main channel (τ = 1.20 ± 0.07 sec) and 200 μm branching channel (τ = 2.37 ± 0.70 sec) also exhibit significantly different τ values (Fig. 11E, $p<0.05$). The phantom that consisted of equal main (τ = 1.30 ± 0.01 sec) and branching (τ = 1.62 ± 0.32 sec) channels of 300 μm diameter, didn't show difference in τ values ($p>0.05$). These values are summarized in Table 4. This suggests that the branching into a smaller vessel is a main parameter that needs to be taken into account when conducting ULM imaging.

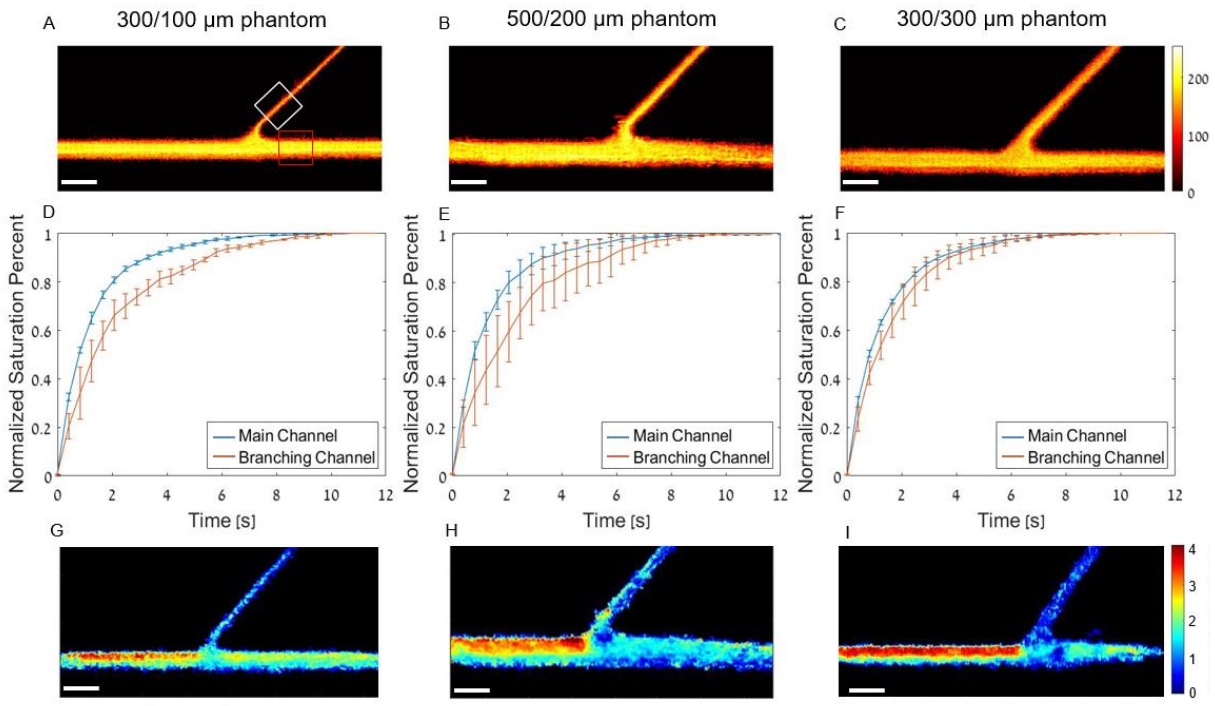

Figure 11. Super-resolved images of phantoms with varying channel widths and saturation time curves. (A) Super-resolved image of phantom with 300 µm main channel and 100 µm branching channel. (B) Super-resolved image of phantom with 500 µm main channel and 200 µm branching channel. (C) Super-resolved image of phantom with 300 µm main and branching channel. All scale bars are 1 mm. (D) Saturation curve for the main and branching channel in the 300/100 µm phantom, P value>0.05. (E) Saturation curve for the main and branching channel in the 500/200 µm phantom, P value > 0.05. (F) Saturation curve for the and branching channel in the 300/300 µm phantom, P value < 0.05. $R^2 > 0.98$ for all fit curves used to calculate τ. (G) Velocity map of the 300/100 µm phantom at a flow rate of 0.01 ml/min. (H) Velocity map of the 500/200 µm phantom at a flow rate of 0.02 ml/min. (I) Velocity map of the 300/300 µm phantom at a flow rate of 0.01 ml/min. All experiments were performed in triplicate, and all data are plotted as ± SD.

Phantom	τ value main channel [sec]	τ value branching channel [sec]
300/100	1.21 ± 0.05	2.09 ± 0.33
500/200	1.20 ± 0.07	2.37 ± 0.70
300/300	1.30 ± 0.01	1.62 ± 0.32

Table 4. Summary of saturation times for various channel widths.

5.4 Trifurcating Phantoms

Lastly, we tested the ability to fabricate complex microvasculature phantoms by creating two trifurcating phantoms. One with a main channel that splits into three channels at equal 30° angles and converges back into one channel (Fig. 12A-C), and one in which the trifurcation splits

equally at 30° angles similarly to the bifurcating phantoms (Fig 12D-F). The converging structure is frequently seen in microfluidic chips and can also mimic the capillary network architecture in-vivo. Super-resolved images and velocity maps were reconstructed for both phantoms. In the velocity maps we see a faster velocity in the main channel before the trifurcation, and then a drop when the channel splits into three (Fig. 12C,F). In the converging phantom, we see a slightly higher velocity in the main channel while in the trifurcating phantom the velocity drops by approximately a factor of three after splitting off from the main channel, as is expected according to conservation of mass equations.

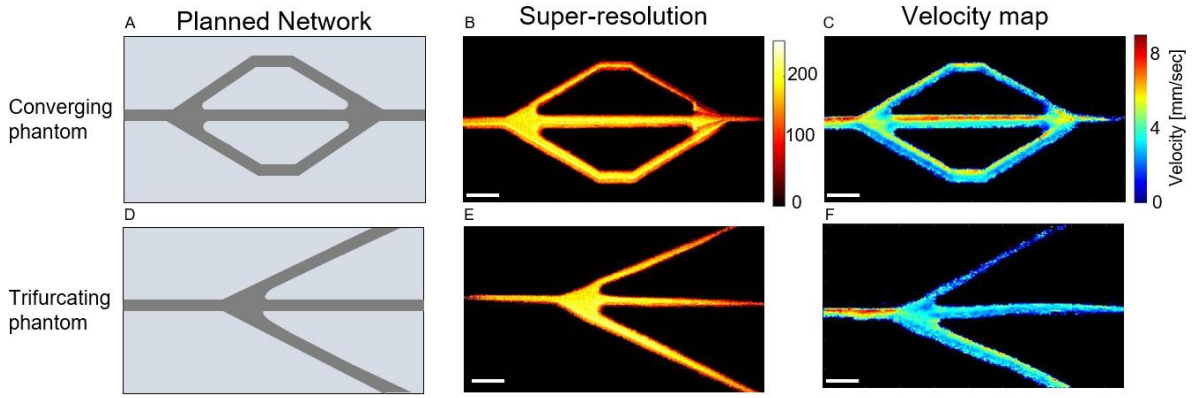

Figure 12. Super-resolved images and velocity maps of trifurcating phantoms. (A) Planned network for microfluidic-style phantom with trifurcating channels that converge back to one main channel. (B) Super-resolved image of converging phantom. (C). Velocity map of converging phantom at a flow rate of 0.02 ml/min. (D) Planned network for trifurcating phantom. (E) Super-resolved image for trifurcating phantom. (F) Velocity map of trifurcating phantom at a flow rate of 0.02 ml/min.

5.5 In vivo saturation time

In order to validate our results seen in phantoms, we compared saturation time between a large and small vessel in in-vivo data obtained from a rat kidney in previous studies [27]. Two vessels were selected from the super resolution image, one with a larger diameter of 410 μm and one with a smaller diameter of 190 μm as seen in the blue and yellow rectangles (Fig. 13). We see that the saturation time of the smaller vessel is slower than that of the larger vessel. This

general trend is in agreement with the results seen in the effect of channel width in previous sections, and with other studies that studied saturation time in ULM images.

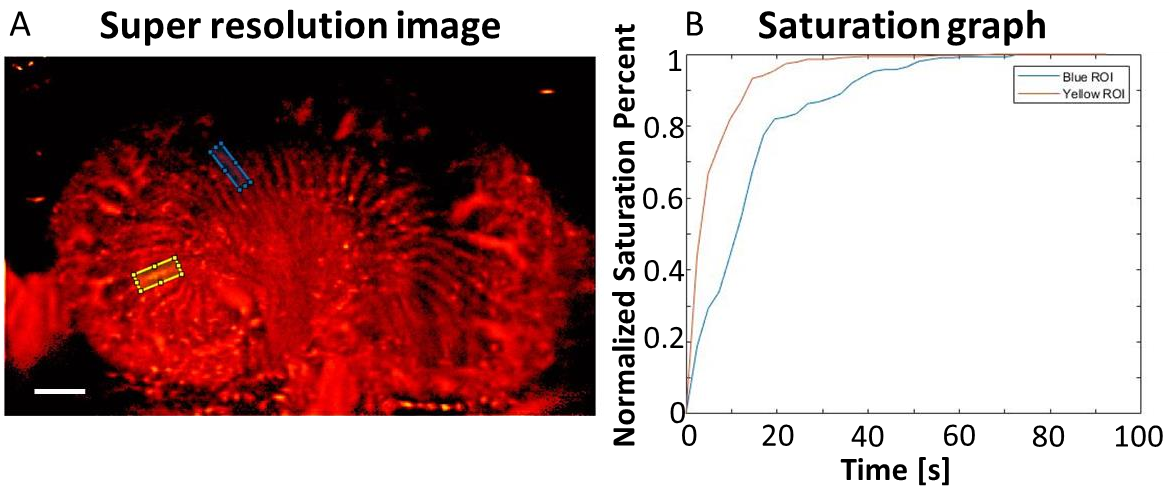

Figure 13. Saturation time of small and large blood vessel in rat kidney. (A) Super resolution image with yellow ROI around a large blood vessel and blue ROI around and small blood vessel. (B) Saturation time curve of the blue and yellow ROI corresponding to a small and large blood vessel in the rat kidney. Velocities within the kidney, not shown, range from 0.5-2 mm/min. Scale bar represents 2 mm. Raw data acquired from [27].

5.6 Preliminary Nanobubble Results – future work

Lastly, the saturation time of MBs and NBs was compared using our phantoms with a main channel width of 300 μm and a branching channel width of 100 μm. NBs have an average diameter of 200 nm, compared to MBs which have a diameter of 1.5-4 μm. The smaller diameter of NBs may affect the physical flow properties, facilitate their entry to smaller blood vessels and improve the required acquisition time of the smaller branching vessel. However, NBs display a weaker signal than MBs and seem more susceptible to radiation force applied by the US wave during data acquisition. This makes imaging them for ULM a challenge that requires optimization of the data acquisition and post processing algorithms. We fabricated echogenic NBs with an average diameter of 200 nm, and performed experiments using identical acquisition parameters as the MBs experiments. Next we compared the saturation time of the branching channel to the

main channel in the phantom with a main channel of 300 µm and a branching channel of 100 µm (Fig.13). MB contrast agents yielded an approximately 30% longer saturation time of the branching channel compared to the main channel. NB contrast agents resulted in no significant difference in saturation time of the main channel compared to the branching channel.

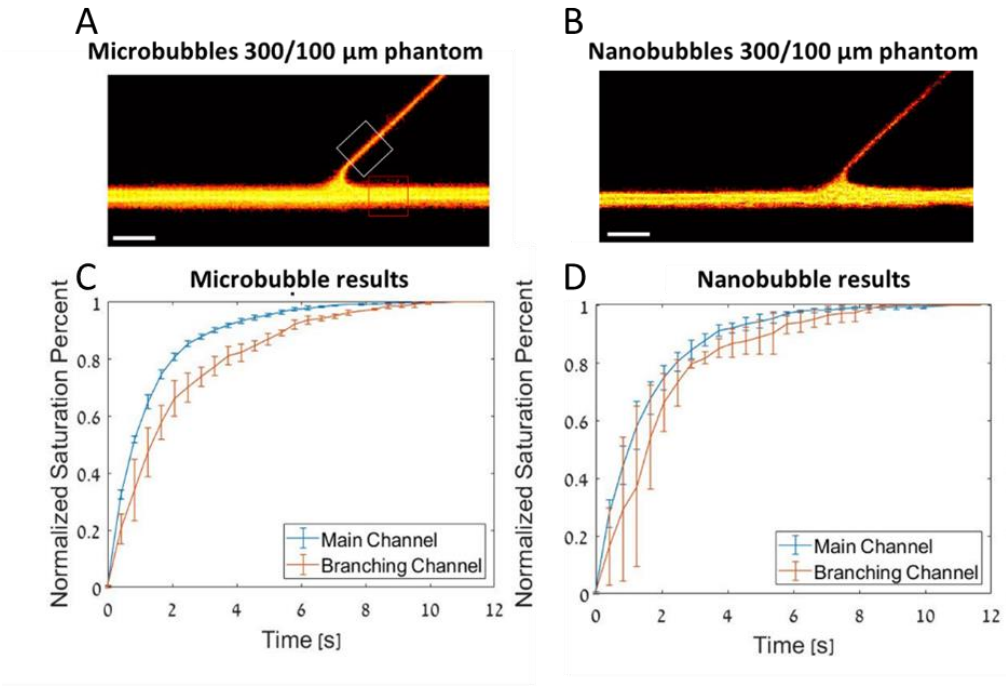

Figure 14. Comparison of saturation time using NBs and MBs in 300/100 µm phantom. (A) Super-resolution image created with MB contrast agents. (B) super-resolution image created with NB contrast agents. (C) Saturation curve of the main and branching channel at 0.02 ml/min using MBs, P value<0.05. (D) Saturation curve of the main and branching channel at 0.02 ml/min using NBs, P value>0.05.

6 Discussion and Conclusions

The aim of this study was to create a fast, simple, and cost effective microfluidic inspired blood vessel mimicking phantom and evaluate the behavior of MBs within bifurcating vessels for ultrasound imaging applications, and specifically for ULM. The vessel mimicking phantoms provide a reproducible network in which behavior of contrast agents and accuracy of tracking algorithms can be compared under multiple controlled conditions. Multiple studies have been conducted regarding contrast agent types [9], [48] and tracking algorithms [8], [25]. We believe

that the development of complex vessel mimicking phantoms can contribute to the fast-growing field of ULM by aiding in understanding of contrast agent behavior and creating a way to systematically test new localization and tracking algorithms. These phantoms may provide an alternative to computerized flow simulations used to evaluate localization and tracking accuracy by creating shapes that are challenging to reproduce with ULM, such as the horseshoe shape [25]. We believe these phantoms can be used to study a wide variety of applications- such as verification of contrast enhanced harmonic imaging, resolution improving ultrasound algorithms, and the behavior of bubble flow in therapeutic applications [45], [49], [50].The method is versatile and can be used to create complex channel phantoms that can aid in understating and characterizing diseases that alter flow patterns such as coronary artery disease, atherosclerosis, inflammation, Crohn's disease, cancer, and kidney diseases [26], [51] The phantom was validated by optimizing MB concentration and calculating velocity through individual MB tracking. Lower MB concentration negatively affected saturation time by producing a lower τ. For ULM, localized PSFs are necessary to ensure accurate localization of contrast agents. Therefore, the concentration was optimized to ensure accuracy in all other experiments. Next, velocity maps for three different flow rates in phantoms with different bifurcation angles showed the expected trend of a faster velocity for a larger flow rate. Velocity in the channels drop by approximately half after the bifurcation. Additionally, the velocity profiles were parabolic as expected for laminar flow within uniform rectangular channels. Interestingly, we see a slight asymmetry in the velocity profiles. We believe this may be due to the radiation force of the ultrasound wave which slightly pushes the bubbles away from the transducer, causing bubbles to slow down as they reach the side of the channel wall. This is apparent in all reconstructed velocity maps and raises the possibility that the flow pattern of MBs may also be affected by the pressure

waves in ultrafast frame rate imaging in vivo. In this case the bubble flow was perpendicular to the wave propagation, making the effect very visible. We find the bifurcation angle of a vessel between 25°-55° to have no significant impact on saturation time when comparing the main channel and branching channel of a phantom. We also find that within the flow rates tested, between 0.01 – 0.03 ml/min, there is no significant difference of saturation time between the main and bifurcation channel.

One of the current ULM challenges is the long acquisition times necessary to reconstruct small blood vessels. Even at ultrafast frame rates of 500 Hz, acquisition time to fully image a rat brain have been reported to take 10 minutes [28]. Studies have shown how slow blood flow and small vessel size negatively affect acquisition time in rat brains, with significant difference in reconstruction time of vessels smaller than 25 μm, vessels between 30-50 μm, and vessels between 70-100 μm [12], [29]. This may be due to a combination of factors. First, the blood flow in capillaries is much slower than in larger vessels, leading to less occurrences of microbubbles in smaller vessels [52]. Additionally, the size of MBs (average diameter of 1.5 - 4 μm) is within the same order of magnitude as capillaries and red blood cells in both animals and humans, further reducing the number of bubbles to flow through capillaries over a set period of time. The platform developed here can be used to study the effect of blood vessel diameter on ULM imaging. Our results show that when a small vessel with a diameter of 100 μm branches off a larger vessel with a diameter of 300 μm, the saturation time of the small vessel is significantly longer than the larger vessel by an average increase of 72%. We also find that in a phantom with a main channel of 500 μm and a branching channel of 200 μm, longer saturation time is required for the smaller branching channel with an average increase of 90%.

The two additional trifurcating phantoms were shown and intended to confirm the robustness of the phantom fabrication method. The phantom that splits and converges back into one channel is especially interesting. This type of configuration is similar to many microfluidic PDMS devices that are readily available (Microfluidic ChipShop, Germany). A benefit of this phantom configuration is the lack of multiple outlets which require equalization of the water pressure to ensure even flow throughout channels. Such ultrasound compatible converging phantom cannot be fabricated using recent reported techniques [35][36][37]. In the velocity maps, we see that the measured velocity in the converging phantom is higher in the middle channel of the trifurcation compared to the two side channels. This may be due to MB dynamics moving through sharper curves and hitting the phantom walls. In the trifurcating phantom that does not converge we see better agreement in the velocity within the three channels.

The in vivo saturation time results align with those observed in our tissue-mimicking phantoms. However, there are some differences between the two datasets. The in vivo data is obtained at a higher frame rate of 300 Hz using a different ultrasound transducer with a center frequency of 6.9 MHz instead of 10 MHz, which is used in our phantom data. Despite these differences, it is evident that larger blood vessels in the rat kidney take longer to saturate compared to smaller ones. A future objective is to capture in vivo data from an elevation where bifurcating vessels are visible in the kidney. This will allow for a comparison of saturation times in a configuration similar to our phantoms. Preliminary NB saturation time results from experiments involving small, bifurcating blood vessels show no significant difference in saturation time compared to the main channel. However, these results need further validation and optimization before being compared to in vivo data using NBs. The NB experiments necessitate using a considerably higher concentration of NBs, with the gas volume being compared instead

of the concentration. Moreover, stronger filtering techniques are required to enhance the weaker NB signal. These steps are necessary to refine the experiments and obtain more accurate data for analysis and comparison.

Regarding the study limitations, in this study, the effect of channel size on MB behavior was examined. In vivo, red blood cells greatly outnumber MBs in the blood stream (approximate concentration of 10^{13}) and therefore may also affect the MB penetration into smaller blood vessels. Additionally, the Fåhræus-Lindqvist effect has a major impact on the viscosity of blood flowing through various sized channels, with blood viscosity decreases as the channel diameter decreases [53]. Therefore, future experiments can be carried out with blood or a blood mimicking fluid to estimate its effect [54]. In these studies, the flow rate throughout data acquisition was kept constant. A pulsatile flow pump may be used to better model the natural flow of blood within the body and study the effects of pulsatile flow under ULM imaging conditions. Additionally, phantoms may be fabricated while taking Murray's law into consideration. Murrays law defines a relationship between radii of blood vessels at junctions within the vascular system, and therefore the radii of branching channels can be calculated to fit this relationship [55]. A cross-linking agent could be added to the gelatin that would allow the phantoms to be maintained at above 37 degrees Celsius, which would enable the study of MBs under physiological conditions. In addition, each specific micro-vascular network mold was fabricated using a CNC machine and cannot be altered. Here we focused on bifurcations and trifurcations stemming from a single channel which is commonly seen in vivo- but different structures such as Y shapes and non-linear channels could be studied. The smallest bifurcation angle of the phantom was limited to 25° due to technical considerations of the CNC drill used. Smaller channels could be created using photolithography to create capillaries and better mimic the shape of blood vessels. This would

come at the additional complication of alignment of two half-circular sections as explained in tissue engineering studies [42].

Additionally, the inlets and outlets of the phantom are created from gelatin which is an elastic material that changes shape under pressure. The pressure from the tubing may change the size of the inlet over time and cause slight leakage of the MB solution. This leakage may affect the flow rate, making it difficult to know the ground truth with complete certainty. This could be addressed by creating more tightly sealed inlets by bonding the hydrogel to glass as suggested in [37]. Lastly, we find that there is a tendency for MBs to get stuck on the channel wall furthest from the US transducer due to the radiation force of the pressure wave. The PSF of these static bubbles may block out the PSF of flowing bubbles, creating an added challenge to tracking bubbles. We find this to have more of an effect in small channel diameters, where the width of the PSF may be larger than the width of the channel. In conclusion, we believe that these micro-vascular phantoms are a robust platform for precise and controlled ULM imaging, and have the potential to be utilized for many diverse aspects of ultrasound imaging.

References

[1] J. L. Prince and J. Links, "Medical Imaging Signals and Systems," *Isbn 0-13-065353-5*. 2014.

[2] P N T Wells, "Ultrasound Imaging," *Phys. Med. Biol 51 R83*, 2006.

[3] R. S. C. Cobbold, "Foundations of Biomedical Ultrasound," *Oxford Univ. Press*, 2007.

[4] T. L. Szabo, *Diagnostic Ultrasound Imaging: Inside Out*. 2004.

[5] F. Tranquart, N. Grenier, V. Eder, and L. Pourcelot, "Clinical use of ultrasound tissue harmonic imaging," *Ultrasound Med. Biol.*, vol. 25, no. 6, 1999, doi: 10.1016/S0301-

5629(99)00060-5.

[6] E. Betzig *et al.*, “Imaging intracellular fluorescent proteins at nanometer resolution,” *Science (80-.).*, vol. 313, no. 5793, 2006, doi: 10.1126/science.1127344.

[7] O. Couture, B. Besson, G. Montaldo, M. Fink, and M. Tanter, “Microbubble ultrasound super-localization imaging (MUSLI),” 2011, doi: 10.1109/ULTSYM.2011.6293576.

[8] P. Song *et al.*, “Improved Super-Resolution Ultrasound Microvessel Imaging with Spatiotemporal Nonlocal Means Filtering and Bipartite Graph-Based Microbubble Tracking,” *IEEE Trans. Ultrason. Ferroelectr. Freq. Control*, vol. 65, no. 2, 2018, doi: 10.1109/TUFFC.2017.2778941.

[9] G. Zhang *et al.*, “Acoustic wave sparsely activated localization microscopy (AWSALM): Super-resolution ultrasound imaging using acoustic activation and deactivation of nanodroplets,” *Appl. Phys. Lett.*, vol. 113, no. 1, 2018, doi: 10.1063/1.5029874.

[10] B. Quan, L. Xiangdong, Z. Shuang, C. Xiang, Z. Xuan, and C. Zeyu, “Detecting Early Ocular Choroidal Melanoma Using Ultrasound Localization Microscopy,” *Bioengineering*, vol. 10, 2023, [Online]. Available: https://doi.org/10.3390/bioengineering10040428.

[11] M. T. Burgess, M. Aliabouzar, C. Aguilar, M. L. Fabiilli, and J. A. Ketterling, “Slow-Flow Ultrasound Localization Microscopy Using Recondensation of Perfluoropentane Nanodroplets,” *Ultrasound Med. Biol.*, vol. 48, no. 5, 2022, doi: 10.1016/j.ultrasmedbio.2021.12.007.

[12] V. Hingot, C. Errico, B. Heiles, L. Rahal, M. Tanter, and O. Couture, "Microvascular flow dictates the compromise between spatial resolution and acquisition time in Ultrasound Localization Microscopy," *Sci. Rep.*, 2019, doi: 10.1038/s41598-018-38349-x.

[13] G. Montaldo, M. Tanter, J. Bercoff, N. Benech, and M. Fink, "Coherent plane-wave compounding for very high frame rate ultrasonography and transient elastography," *IEEE Trans. Ultrason. Ferroelectr. Freq. Control*, vol. 56, no. 3, 2009, doi: 10.1109/TUFFC.2009.1067.

[14] J. Jensen, "Fast Plane Wave Imaging," *Citation*, 2020.

[15] P. J. Phillips, "Contrast pulse sequences (CPS): Imaging nonlinear microbubbles," 2001, doi: 10.1109/ultsym.2001.992057.

[16] G. ter Haar, "Ultrasonic imaging: Safety considerations," *Interface Focus*, vol. 1, no. 4. 2011, doi: 10.1098/rsfs.2011.0029.

[17] I. Karagoz and M. K. Kartal, "Evaluation of nonscanned mode soft-tissue thermal index in the presence of the residual temperature rise," *Ultrasound Med. Biol.*, vol. 32, no. 5, 2006, doi: 10.1016/j.ultrasmedbio.2006.02.1404.

[18] T. Şen, O. Tüfekçioğlu, and Y. Koza, "Mechanical index," *Anadolu Kardiyol. Derg.*, vol. 15, no. 4, 2015, doi: 10.5152/akd.2015.6061.

[19] M. U. Aziz *et al.*, "Microvascular Flow Imaging: A State-of-the-Art Review of Clinical Use and Promise," *Radiology*, vol. 305, no. 2. 2022, doi: 10.1148/radiol.213303.

[20] C. Molnar and J. Gair, *CONCEPTS OF BIOLOGY*, 1st ed. BCcampus, 2015.

[21] C. Lal and M. J. Leahy, “An Updated Review of Methods and Advancements in Microvascular Blood Flow Imaging,” *Microcirculation*, vol. 23, no. 5. 2016, doi: 10.1111/micc.12284.

[22] R. W. Gill, “Measurement of blood flow by ultrasound: Accuracy and sources of error,” *Ultrasound Med. Biol.*, vol. 11, no. 4, 1985, doi: 10.1016/0301-5629(85)90035-3.

[23] G. Hong *et al.*, “Multifunctional in vivo vascular imaging using near-infrared II fluorescence,” *Nat. Med.*, vol. 18, no. 12, 2012, doi: 10.1038/nm.2995.

[24] C. H. Huang *et al.*, “High-resolution structural and functional assessments of cerebral microvasculature using 3D gas ΔR2*-mMRA,” *PLoS One*, vol. 8, no. 11, 2013, doi: 10.1371/journal.pone.0078186.

[25] B. Heiles, A. Chavignon, V. Hingot, P. Lopez, E. Teston, and O. Couture, “Performance benchmarking of microbubble-localization algorithms for ultrasound localization microscopy,” *Nat. Biomed. Eng.*, 2022, doi: 10.1038/s41551-021-00824-8.

[26] O. Couture, V. Hingot, B. Heiles, P. Muleki-Seya, and M. Tanter, “Ultrasound localization microscopy and super-resolution: A state of the art,” *IEEE Trans. Ultrason. Ferroelectr. Freq. Control*, 2018, doi: 10.1109/TUFFC.2018.2850811.

[27] J. Foiret, H. Zhang, T. Ilovitsh, L. Mahakian, S. Tam, and K. W. Ferrara, “Ultrasound localization microscopy to image and assess microvasculature in a rat kidney,” *Sci. Rep.*, vol. 7, no. 1, 2017, doi: 10.1038/s41598-017-13676-7.

[28] C. Errico *et al.*, “Ultrafast ultrasound localization microscopy for deep super-resolution vascular imaging,” *Nature*, 2015, doi: 10.1038/nature16066.

[29] N. Renaudin, C. Demene, A. Dizeux, N. Laly-Radoi, S. Pezet, and M. Tanter, "Functional ultrasound localization microscopy reveals brain-wide neurovascular activity on a microscopic scale," *Nat. Methods*, 2022, [Online]. Available: https://doi.org/10.1038/s41592-022-01549-5.

[30] M. A. O'Reilly and K. Hynynen, "A super-resolution ultrasound method for brain vascular mapping," *Med. Phys.*, vol. 40, no. 11, 2013, doi: 10.1118/1.4823762.

[31] X. Zhao, A. Write, and D. E. Goertz, "An optical and acoustic investigation of microbubble cavitation in small chan- nels under therapeutic ultrasound conditions," *Ultrason. Sonochem.*, 2023, doi: https://doi.org/10.1016/j.ultsonch.2023.106291.

[32] C. F. Caskey, D. E. Kruse, P. A. Dayton, T. K. Kitano, and K. W. Ferrara, "Microbubble oscillation in tubes with diameters of 12, 25, and 195 microns," *Appl. Phys. Lett.*, vol. 88, no. 3, 2006, doi: 10.1063/1.2164392.

[33] C. Demené *et al.*, "Spatiotemporal Clutter Filtering of Ultrafast Ultrasound Data Highly Increases Doppler and fUltrasound Sensitivity," *IEEE Trans. Med. Imaging*, vol. 34, no. 11, 2015, doi: 10.1109/TMI.2015.2428634.

[34] E. Candes, X. L. J., M. Yi, and J. Wright, "Robust principle component analysis?," *J. ACM*, vol. 58, no. 3, pp. 1–37, 2011.

[35] S. J. Paulsen *et al.*, "Projection-based stereolithography for direct 3D printing of heterogeneous ultrasound phantoms," *PLoS One*, vol. 16, no. 12 December, 2021, doi: 10.1371/journal.pone.0260737.

[36] M. L. Ommen *et al.*, "3D Printed Flow Phantoms with Fiducial Markers for Super-

Resolution Ultrasound Imaging," in *IEEE International Ultrasonics Symposium, IUS*, 2018, vol. 2018-October, doi: 10.1109/ULTSYM.2018.8580217.

[37] S. Kawara, B. Cunningham, J. Beser, N. Kc, and S. H. Au, "Capillary-Scale Hydrogel Microchannel Networks by Wire Templating," *Small*, vol. 2301164, 2023.

[38] R. P. Zangabad *et al.*, "Ultrasonic characterization of ibidi μ-Slide I Luer channel slides for studies with ultrasound contrast agents," *IEEE Trans. Ultrason. Ferroelectr. Freq. Control*, 2023.

[39] P. Chen *et al.*, "Acoustic characterization of tissue-mimicking materials for ultrasound perfusion imaging research," *Ultrasound Med. Biol.*, vol. 48, no. 1, 2022, doi: 10.1016/j.ultrasmedbio.2021.09.004.

[40] O. M. Viessmann, R. J. Eckersley, K. Christensen-Jeffries, M. X. Tang, and C. Dunsby, "Acoustic super-resolution with ultrasound and microbubbles," *Phys. Med. Biol.*, vol. 58, no. 18, 2013, doi: 10.1088/0031-9155/58/18/6447.

[41] X. Qian *et al.*, "Super-Resolution Ultrasound Localization Microscopy for Visualization of the Ocular Blood Flow," *IEEE Trans. Biomed. Eng.*, vol. 69, no. 5, 2022, doi: 10.1109/TBME.2021.3120368.

[42] J. He *et al.*, "Fabrication of circular microfluidic network in enzymatically-crosslinked gelatin hydrogel," *Mater. Sci. Eng. C*, 2016, doi: 10.1016/j.msec.2015.09.104.

[43] R. Chen, B. Wang, Y. Liu, J. He, R. Lin, and D. Li, "Gelatin-based perfusable, endothelial carotid artery model for the study of atherosclerosis," *Biomed. Eng. Online*, 2019, doi: 10.1186/s12938-019-0706-6.

[44] T. Ilovitsh *et al.*, “Enhanced microbubble contrast agent oscillation following 250 kHz insonation,” *Sci. Rep.*, vol. 8, no. 1, 2018, doi: 10.1038/s41598-018-34494-5.

[45] K. T. Karlinsky and T. Ilovitsh, “Ultrasound Frequency Mixing for Enhanced Contrast Harmonic Imaging of Microbubbles,” *IEEE Trans. Ultrason. Ferroelectr. Freq. Control*, vol. 69, no. 8, 2022, doi: 10.1109/TUFFC.2022.3179471.

[46] M. Bismuth, S. Katz, H. Rosenblatt, M. Twito, R. Aronovich, and T. Ilovitsh, “Acoustically Detonated Microbubbles Coupled with Low Frequency Insonation: Multiparameter Evaluation of Low Energy Mechanical Ablation,” *Bioconjug. Chem.*, vol. 33, no. 6, 2022, doi: 10.1021/acs.bioconjchem.1c00203.

[47] C. Dong, C. C. Loy, and X. Tang, “Accelerating the super-resolution convolutional neural network,” in *Lecture Notes in Computer Science (including subseries Lecture Notes in Artificial Intelligence and Lecture Notes in Bioinformatics)*, 2016, vol. 9906 LNCS, doi: 10.1007/978-3-319-46475-6_25.

[48] G. Zhang *et al.*, “Fast acoustic wave sparsely activated localization microscopy: Ultrasound super-resolution using plane-wave activation of nanodroplets,” *IEEE Trans. Ultrason. Ferroelectr. Freq. Control*, vol. 66, no. 6, 2019, doi: 10.1109/TUFFC.2019.2906496.

[49] R. Abiteboul and T. Ilovitsh, “Optimized Simultaneous Axial Multifocal Imaging via Frequency Multiplexed Focusing,” *IEEE Trans. Ultrason. Ferroelectr. Freq. Control*, vol. 69, no. 10, 2022, doi: 10.1109/TUFFC.2022.3200468.

[50] B. Glickstein, R. Aronovich, Y. Feng, and T. Ilovitsh, “Development of an ultrasound guided focused ultrasound system for 3D volumetric low energy nanodroplet-mediated

histotripsy," *Sci. Rep.*, vol. 12, no. 1, 2022, doi: 10.1038/s41598-022-25129-x.

[51] E. Falk, "Pathogenesis of Atherosclerosis," *Journal of the American College of Cardiology*, vol. 47, no. 8 SUPPL. 2006, doi: 10.1016/j.jacc.2005.09.068.

[52] K. P. Ivanov, M. K. Kalinina, and Y. I. Levkovich, "Blood flow velocity in capillaries of brain and muscles and its physiological significance," *Microvasc. Res.*, 1981, doi: 10.1016/0026-2862(81)90084-4.

[53] R. Chebbi, "Dynamics of blood flow: modeling of the Fåhræus–Lindqvist effect," *J. Biol. Phys.*, vol. 41, no. 3, 2015, doi: 10.1007/s10867-015-9376-1.

[54] E. Bianconi *et al.*, "An estimation of the number of cells in the human body," *Ann. Hum. Biol.*, vol. 40, no. 6, 2013, doi: 10.3109/03014460.2013.807878.

[55] C. D. Murray, "The Physiological Principle of Minimum Work: I. The Vascular System and the Cost of Blood Volume.," *Proc. Natl. Acad. Sci. U. S. A.*, vol. 12, no. 3, 1926, doi: 10.1073/pnas.12.3.207.

אוניברסיטת תל אביב

הפקולטה להנדסה ע"ש איבי ואלדר פליישמן

בית הספר לתארים מתקדמים ע"ש זנדמן-סליינר

פיתוח התקן מדמה רקמה לחקר זרימה מיקרו-וסקולרית והדמיית סופר רזולוציה באמצעות אולטרסאונד

חיבור זה הוגש כעבודת גמר לקראת התואר "מוסמך אוניברסיטה" בהנדסה ביו-רפואית

על-ידי

תמר מנו

העבודה נעשתה במחלקה להנדסה ביו-רפואית

בהנחיית ד"ר טלי אילוביץ

אוניברסיטת תל אביב

הפקולטה להנדסה ע"ש איבי ואלדר פליישמן

בית הספר לתארים מתקדמים ע"ש זנדמן-סליינר

פיתוח התקן מדמה רקמה לחקר זרימה מיקרו-וסקולרית והדמיית סופר רזולוציה באמצעות אולטרסאונד

חיבור זה הוגש כעבודת גמר לקראת התואר "מוסמך אוניברסיטה" בהנדסה ביו-רפואית

על-ידי

תמר מנו

העבודה נעשתה במחלקה להנדסה ביו-רפואית

בהנחיית ד"ר טלי אילוביץ